Hydroxyapatite−TiO$_2$-based Nanocomposites Synthesized in Supercritical CO$_2$ for Bone Tissue Engineering: Physical and Mechanical Properties

Mehrnaz Salarian,[†] William Z. Xu,[‡] Zhiqiang Wang,[§] Tsun-Kong Sham,[§,||] and Paul A. Charpentier*,[‡]

[†]Biomedical Engineering Graduate Program, University of Western Ontario, London, Ontario N6A 5B9, Canada
[‡]Chemical and Biochemical Engineering Department, University of Western Ontario, London, Ontario N6A 5B9, Canada
[§]Department of Chemistry, University of Western Ontario, London, Ontario N6A 5B7, Canada
[||]Soochow−Western Centre for Synchrotron Radiation Research, University of Western Ontario, London, Ontario N6A 5B7, Canada

ABSTRACT: Calcium phosphate-based nanocomposites offer a unique solution toward producing scaffolds for orthopedic and dental implants. However, despite attractive bioactivity and biocompatibility, hydroxyapatite (HAp) has been limited in heavy load-bearing applications due to its intrinsically low mechanical strength. In this work, to improve the mechanical properties of HAp, we grew HAp nanoplates from the surface of one-dimensional titania nanorod structures by combining a coprecipitation and sol−gel methodology using supercritical fluid processing with carbon dioxide (scCO$_2$). The effects of

metal alkoxide concentration (1.1−1.5 mol/L), reaction temperature (60−80 °C), and pressure (6000−8000 psi) on the morphology, crystallinity, and surface area of the resulting nanostructured composites were examined using scanning electron microscopy (SEM), transmission electron microscopy (TEM), powder X-ray diffraction (XRD), and Brunauer−Emmet−Teller (BET) method. Chemical composition of the products was characterized using Fourier transform infrared (FTIR) spectroscopy, X-ray photoelectron spectroscopy (XPS), and X-ray absorption near-edge structure (XANES) analyses. HAp nanoplates and HAp−TiO$_2$ nanocomposites were homogeneously mixed within poly(ε-caprolactone) (PCL) to develop scaffolds with enhanced physical and mechanical properties for bone regeneration. Mechanical behavior analysis demonstrated that the Young's and flexural moduli of the PCL/HAp−TiO$_2$ composites were substantially higher than the PCL/HAp composites. Therefore, this new synthesis methodology in scCO$_2$ holds promise for bone tissue engineering with improved mechanical properties.

KEYWORDS: hydroxyapatite−titania nanocomposite, morphology, supercritical carbon dioxide, sol−gel method, mechanical properties
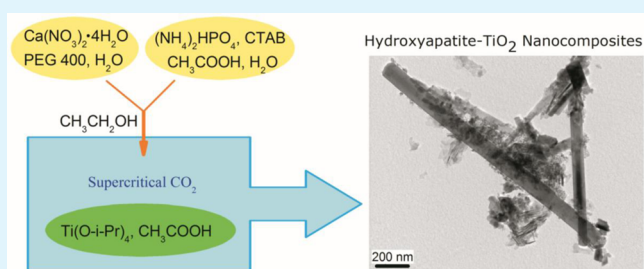
1. INTRODUCTION

Hydroxyapatite (Ca$_{10}$(PO$_4$)$_6$(OH)$_2$, HAp) nanoparticles have attracted great interest, as their chemical and crystallographic structure is similar to the mineral phase of the human hard tissues, bone and teeth.[1] HAp has shown excellent biocompatibility, bioactivity, and high osteo-conductivity and therefore has been used in reconstructive and prosthetic materials for bone and teeth.[1−3] However, the principal limitations in the clinical use of pure HAp as a load bearing implant are its intrinsic brittleness and poor mechanical properties in the presence of body fluids and under local loading.[4,5] Generally, the size and morphology of the HAp particles have a direct influence on their ability to reinforce materials.[6] Mechanical properties of these HAp-based materials can potentially be improved by integrating one-dimensional (1D) nanostructures, including nanorods, nanofibers, or nanotubes.[7,8] It was previously shown that the morphology and size of HAp particles could be controlled by the presence of cetyltrimethylammonium bromide (CTAB) and polyethylene glycol (PEG) under hydrothermal conditions.[9,10] Nevertheless, it is very challenging

to prepare HAp nanogeometries, as HAp nanoparticles tend to agglomerate.[5]

Immobilization of a biocompatible metal oxide, such as Al$_2$O$_3$, ZrO$_2$, SiO$_2$, and TiO$_2$, on the surface of the hydroxyapatite can potentially enhance the mechanical properties of HAp, along with enhancing biocompatibility and cellular response.[11,12] Among these HAp-based composites, HAp−TiO$_2$ composites have attracted considerable attention due to the combined advantages of both materials. Namely, TiO$_2$ is capable of enhancing osteoblast adhesion[13] and inducing cell growth[14] with living tissue, while HAp is biocompatible. HAp−TiO$_2$ composite materials have recently been shown to enhance load-bearing biomedical applications[15,16] while also being beneficial in antibacterial applications.[17]
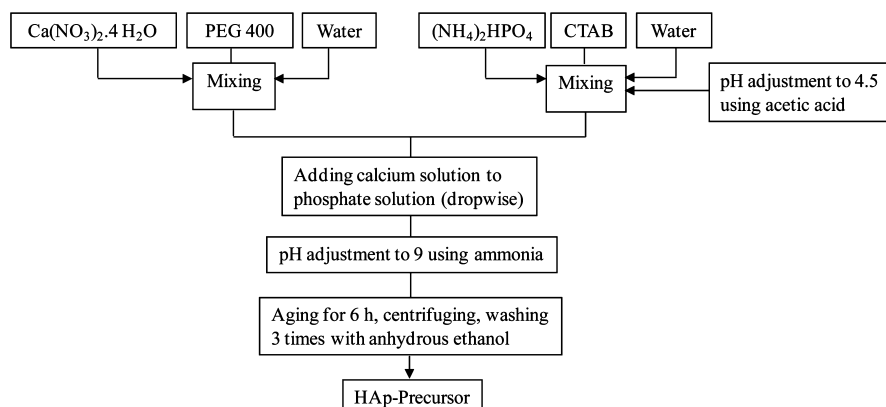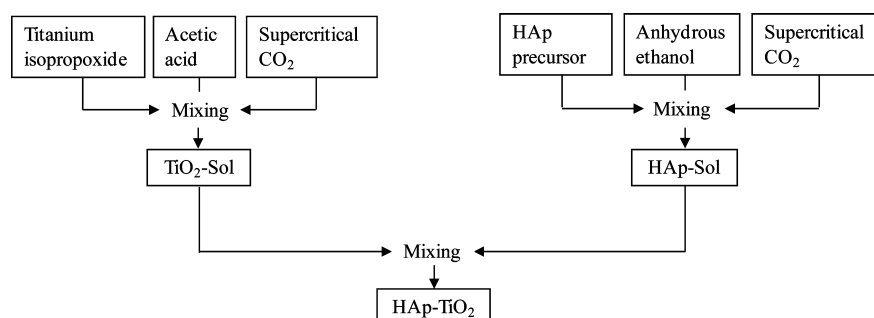
HAp−TiO$_2$ composites have been prepared by different methods such as sol−gel,[18,19] hydrothermal,[20] combined gravity/hydrothermal

Scheme 1. Schematic Representation of the Preparation of HAp Precursor

Scheme 2. Schematic Representation of Sol−Gel Process for Producing HAp−TiO$_2$ Composites

processing,[5] electrospinning,[16] microwave-assisted coprecipitation process,[11,21] and so on. However, obtaining a crystalline powder in most of these methods requires costly heat treatment at high temperatures or for long reaction periods. They also suffer scale-up problems[11] and are not environmentally friendly. Consequently, a more efficient synthetic methodology would be useful to prepare HAp−TiO$_2$ composites. Previously, direct sol−gel reactions in supercritical carbon dioxide (scCO$_2$) have attracted much attention for synthesizing oxide nanomaterials of unique morphologies.[22,23] Recently, the Charpentier group introduced a one-step sol−gel method to prepare TiO$_2$ nanofibers and ZrO$_2$-modified TiO$_2$ nanotubes where scCO$_2$ was used as the functional solvent for both self-assembly and as the drying agent.[24,25] This method provides several advantages to tailoring the nanomorphology by simply "tuning" the supercritical fluids temperature and pressure.[24,26] Moreover, any unreacted starting materials can be safely removed from the synthesized products by supercritical fluid extraction (SFE) during the cleaning process, maintaining the porous nanostructure of the products while providing clean products suitable for biomedical applications.[25,26]

The aim of this study was to develop a new synthetic procedure for the synthesis of HAp−TiO$_2$ nanocomposites by combining coprecipitation and sol−gel method in scCO$_2$. The nanosized HAp−TiO$_2$ particles are examined as a reinforcing phase in polycaprolactone (PCL) matrix. PCL is a biocompatible and bioresorbable polyester commonly used in medical and drug delivery applications.[27,28] The degradation kinetics and preservation of the mechanical properties make PCL an excellent candidate as a temporary joint spacer in total joint prostheses.[29] In addition, X-ray absorption near-edge structure (XANES) spectroscopy that probes the local structure and bonding of the absorbing atoms using tunable X-rays from a synchrotron light source was applied to study the composition of the HAp−TiO$_2$ nanoparticles, showing that the weight ratio between anatase TiO$_2$ and HAp is about 1:1.6. These nanosized PCL/HAp−TiO$_2$ composites are encouraging for the preparation of scaffolds for next generation bone tissue engineering applications.

2. EXPERIMENTAL SECTION

2.1. Materials. Calcium nitrate tetrahydrate (Ca(NO$_3$)$_2$·4H$_2$O), diammonium hydrogen phosphate ((NH$_4$)$_2$HPO$_4$), cetyltrimethylammonium bromide (CTAB), and polyethylene glycol PEG 400 were obtained from Sigma-Aldrich, Canada. All chemicals were of analytical grade or higher and used as received. Titanium isopropoxide (TIP, 99.999%) trace metals basis, glacial acetic acid (>99.7%), ammonium hydroxide (NH$_4$OH, 30%), dichloromethane (DCM, 99.5%), anhydrous ethanol (EtOH), and polycaprolactone (PCL) (MW 80 000 g/mol) were purchased from Sigma-Aldrich, Canada, and used as received.

2.2. Methods. *2.2.1. Preparation of HAp Nanoparticles Using a Combined Coprecipitation and Sol−Gel Method.* The Ca^{2+}/PO$_4^{3-}$ molar ratio of the reactants was maintained at a stoichiometric ratio of HAp (1.67). The general procedure is as follows: First, (NH$_4$)$_2$HPO$_4$ (1.078 g, 0.008 mol) and CTAB (2.083 g, 0.0056 mol) were dissolved in 33.3 mL of deionized water. The solution was stirred for 30 min with a magnetic stirrer, and then the pH value was adjusted to 4.5 by adding pure acetic acid. After this, Ca(NO$_3$)$_2$·4H$_2$O (3.228 g, 0.0135 mol) was dissolved in 46.67 mL of DI water and 6.67 mL of PEG 400 was added at the same time with constant stirring for 20 min. Afterward, the Ca(NO$_3$)$_2$·4H$_2$O + PEG 400 solution was added to the (NH$_4$)$_2$HPO$_4$ + CTAB solution dropwise while stirring. Dropwise addition of ammonia was used to adjust the pH of the solution to 9. The resulting white suspension was then stirred at room temperature for 6 h and centrifuged to separate the precipitates from the suspension, followed by washing three times with ethanol to remove the remaining CTAB and PEG 400. This procedure gave the HAp precursor as described in Scheme 1. To synthesize the HAp nanoplates in scCO$_2$,

Table 1. Experimental Conditions for HAp and HAp–TiO$_2$ Nanostructure Formation and Characterization Results (Morphology and BET Surface Area)

	temperature (°C)	pressure (psi)	$C_{0\,(TIP)}$ (mol l^{-1})	(AcOH/TIP) weight ratio	BET (m^2 g^{-1})	morphology
TiO$_2$	60	6000	1.1	4	111	nanofiber–nanotube
HAp-1	60	6000			60	nanoplate
HAp-2	80	6000			72	nanoplate
HAp–TiO$_2$-1	80	6000	1.1	4	100	nanoplate–thick sheet-type structure
HAp–TiO$_2$-2	80	6000	1.5	4	170	nanoplate on the surface of nanorods
HAp–TiO$_2$-3	80	8000	1.5	4	108	nanoplate–nanorods
HAp–TiO$_2$-h	Hydrothermal treatment at 200 °C for 24 h				98	oblong-shaped

the HAp precursor (3 g) was dispersed in ethanol at a 1:1 weight ratio while vigorously stirring and placed in a 10 mL stainless steel view cell reactor, followed by the addition of CO$_2$ using a high-pressure syringe pump (Isco 260D). The schematic diagram of the experimental setup was previously provided in Sui et al.,[23] with the temperature and pressure effects examined in this work. The precursor was stirred for 24 h, and 4–5 days of aging was provided for additional reaction completion. The obtained gel was then washed with CO$_2$, followed by controlled venting, then kept under vacuum at 80 °C to remove any remaining moisture or volatiles.

2.2.2. Preparation of HAp–TiO$_2$ Nanocomposites Using a Combined Coprecipitation and Sol–Gel Method. In a typical experiment, the HAp precursor (1.5 g), prepared following the procedure in section 2.2.1, was dispersed in ethanol (1.5 g) and placed in a 10 mL high-pressure view cell, followed by quick addition of titanium isopropoxide (1 g) and acetic acid (4 g), and heated/pressurized with CO$_2$ to the desired temperature and pressure. A TFE stir bar was used for mixing the reaction mixture. The mixture of HAp precursor, titanium isopropoxide, and acetic acid was dispersed in scCO$_2$ at the studied temperature 80 °C and pressure range from 6000 to 8000 psi. The reaction was kept under continuous stirring for 24 h, and 5–6 days of aging were necessary for additional reaction completion, as shown in Scheme 2. After aging, the formed gel was washed with CO$_2$ followed by controlled venting. The resultant powders were kept under vacuum at 80 °C, then calcined at 500 °C in air for 2 h using a heating rate of 10 °C/min and a cooling rate of 0.5 °C/min to room temperature.

For comparison of XANES study, TiO$_2$ nanoparticles were synthesized following the procedure presented in Salarian et al.[30] and calcined at 450 and 750 °C.

2.2.3. Preparation of HAp–TiO$_2$ Nanocomposites Using Hydrothermal Technique. Similar to the synthesis of the HAp precursor, (NH$_4$)$_2$HPO$_4$ (1.213 g, 0.009 mol) and CTAB (2.343 g, 0.0063 mol) were dissolved in 37.5 mL of deionized water, and the solution was stirred for 30 min with a magnetic stirrer followed by adjusting the pH value to 4.5 using acetic acid. After that, Ca(NO$_3$)$_2$·4H$_2$O (3.632 g, 0.0152 mol) was dissolved in 52.5 mL of deionized water, and 7.5 mL of PEG 400 was simultaneously added to the solution while the solution was stirred for 20 min. Then, the Ca(NO$_3$)$_2$·4H$_2$O + PEG 400 solution was added to the (NH$_4$)$_2$HPO$_4$ + CTAB solution dropwise with constant stirring. Simultaneously, TIP (1 g) was mixed with acetic acid (6 g) and added dropwise to the reaction media (phosphate solution). Ammonia was used to adjust the solution pH to 11. The final suspension was transferred to a 125 mL stainless steel autoclave and then hydrothermally treated at 200 °C for 24 h. After reaction, any precipitates were separated from the suspension by centrifugation at 5000 rpm for 10 min, washed three times with ethanol, and freeze-dried to yield the product (white powder).

2.2.4. PCL/HAp–TiO$_2$ and PCL/HAp Composite Preparation. To produce PCL/HAp composites, we dispersed HAp powders synthesized in scCO$_2$ in dichloromethane by mixing for 15 min and then sonicated the mixture for 5 min. PCL was added to the HAp/DCM suspension containing the PCL:HAp (w/w) ratios of 90:10, 80:20, and 70:30. The resulting slurries were cast onto clean glass dishes and allowed to evaporate in air. The produced PCL/HAp films were heat-pressed at 100 °C using 670 N of force for 2 min. To prepare PCL/HAp–TiO$_2$ specimens, we applied the same procedure

using the HAp–TiO$_2$ powders synthesized by combined coprecipitation and sol–gel method and hydrothermal treatment.

2.3. Characterization. The morphologies of the samples were studied using scanning electron microscopy (SEM, Hitachi S-4500) and transmission electron microscopy (TEM, JEOL 2010F) with a 200 keV Schottky field emission microscope (TEM/STEM). The bulk composition and elemental analysis of the HAp–TiO$_2$ powders was analyzed using energy-dispersive Quartz XOne X-ray spectroscopy (EDX) attached to a Hitachi S-4500 field emission SEM on three fields of view (n = 3). Structural analysis of the powders was performed using an Inel powder diffractometer equipped with a Cu-X-ray radiation tube, an Inel XRG3000 generator, and an Inel CPS 120 detector. The diffraction pattern data was processed with the IMAD program and the MATCH software, which was used for phase identification from the powder diffraction data. The ICDD PDF4+ database was used to search for reference patterns. TGA was carried out to study the thermal decomposition behavior of the HAp and HAp–TiO$_2$ nanocomposites. TGA analysis of the synthesized nanostructures was performed using a thermogravimetric analyzer, TA Instrument (TA-Q500), at a heating rate of 10 °C/min from room temperature to 1200 °C under flowing air. X-ray photoelectron spectroscopy (XPS) analyses were carried out with a Kratos Axis Ultra spectrometer using a monochromatic Al Kα source (15 mA, 14 kV). Samples were mounted on a nonconductive double-sided adhesive tape with a Kratos charge neutralizer system used on all specimens. Survey scan analyses were carried out with an analysis area of 300 × 700 μm and a pass energy of 160 eV. Spectra were charge corrected to the main line of the carbon 1s spectrum set to 284.8 eV, then analyzed using CasaXPS software (version 2.3.14). Synchrotron measurements were carried out at the high-resolution spherical grating monochromator (SGM) beamline at the Canadian Light Source (CLS), University of Saskatchewan. The samples were mounted on conventional carbon tapes with an angle of 20° facing toward the photon beam. XANES spectra were recorded in total electron yield (TEY) that was detected with the specimen current. All XANES spectra were normalized to the incident photon flux collected on a refreshed Au grid. The Fourier transform infrared (FTIR) spectra of the samples were collected using a Bruker IFS 55 FTIR instrument with an attached MCT detector. Samples (4 wt %) were mixed with potassium bromide (KBr), then pressed into pellets. The spectra were recorded within the range of 400–4000 cm^{-1} with a resolution of 4 cm^{-1} over 32 scans. The specific surface areas and the average pores size of the powders were determined via Brunauer–Emmet–Teller (BET) method and Barret–Joyner–Halenda (BJH) analysis of BET isotherms using Tristar II 3020 (Micromeritics Instrument Corporation). All the samples were degassed at 150 °C for 12 h.

2.4. Mechanical Behavior Analyses of PCL/HAp–TiO$_2$ and PCL/HAp Composites. Tensile properties of PCL/HAp–TiO$_2$ and PCL/HAp composites were measured using a universal testing machine (Instron 5943) with a 500 N load cell. For tensile testing, dogbone specimens with overall length of 60 mm and width of grip section of 10 mm were used. To prepare the specimens, a stainless steel mold was loaded with slices of PCL/HAp and PCL/HAp–TiO$_2$ films. The stainless steel mold was then heated at 100 °C for 30 min and heat-pressed for 2 min at 100 °C and 670 N. Prepared specimens were soaked in deionized (DI) water for 24 h at 37 °C before testing. Stress–strain relationships were obtained from the load and displacement
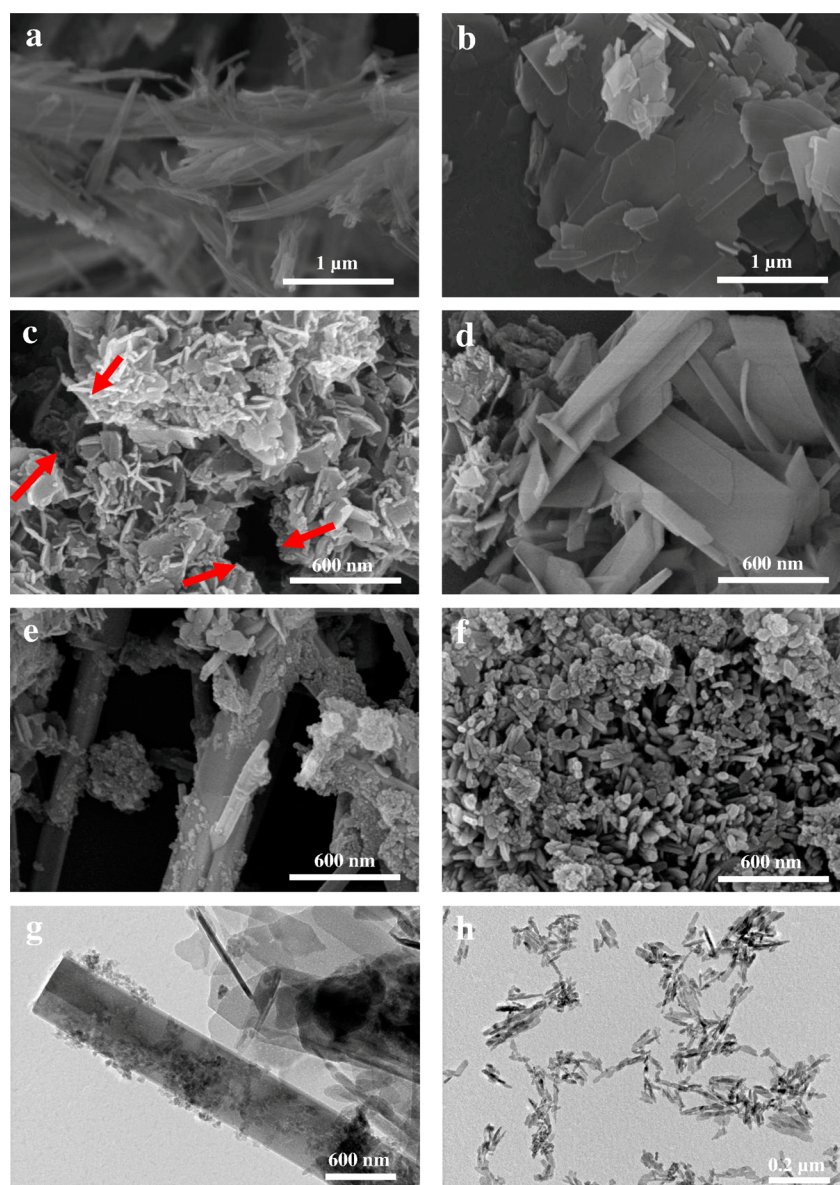
16920

dx.doi.org/10.1021/am5044888 | *ACS Appl. Mater. Interfaces* 2014, 6, 16918–16931

Figure 1. SEM images of the (a) TiO$_2$ nanotubes calcined at 450 °C, (b) as-prepared HAp-1 nanoplates, (c) as-prepared HAp-2 nanoplates, (d) HAp−TiO$_2$-1 nanocomposites calcined at 500 °C, (e) HAp−TiO$_2$-2 nanocomposites calcined at 500 °C, and (f) HAp−TiO$_2$-h nanocomposites. TEM images of (g) HAp−TiO$_2$-2 nanocomposites calcined at 500 °C and (h) HAp−TiO$_2$-h nanocomposites. Arrows in panel c indicate the voids between aggregates of plate-like HAp secondary particles.

data. The Young's modulus was determined by calculating the slope of the linear portion of the stress−strain curve, and the tensile strength was defined as the maximum stress achieved. Flexural strength (FS) and flexural modulus (FM) of the samples were measured in accordance with ASTM D790M-92 ($n = 5$) using a dynamic mechanical analyzer (DMA Q800, TA Instruments) with a crosshead speed of 10 mm/min. For flexural testing, rectangular bar specimens ($n = 5$; $50 \times 25 \times 2$ mm), were prepared using the stainless steel mold heat-pressed following the same procedure as tensile testing specimens. Prepared samples were soaked in DI water for 24 h at 37 °C before testing. Flexural moduli were calculated as the slope of the initial linear region of the stress−strain curve, where the flexural fracture strength was determined as the maximum applied stress prior to failure.

3. RESULTS AND DISCUSSION

3.1. SEM and TEM Characterization of the As-Synthesized HAp and Calcined HAp−TiO$_2$ Composites Powders. The experimental conditions and characterization results for the

as-synthesized HAp and calcined HAp−TiO$_2$ composites powders are provided in Table 1.

SEM micrographs of the synthesized materials (Figure 1a−f) and TEM images of HAp−TiO$_2$-2 and HAp−TiO$_2$-h nanocomposite (Figure 1g,h) show that the HAp and HAp−TiO$_2$ composites powders were composed of various nanostructures. SEM image of the TiO$_2$ nanoparticles calcined at 450 °C is shown in Figure 1a, indicating the formation of tubelike and fiberlike structures. More detailed information on the experimental procedure of these TiO$_2$ nanoparticles are presented in Salarian et al.[30] Figure 1b,c shows the platelike particles of samples HAp-1 (150−250 nm in width) and HAp-2 (40−100 nm in width), synthesized in scCO$_2$ using a pressure of 6000 psi at 60 and 80 °C, respectively. In general, we found slight changes in the morphology and dimensions of the particulates when the reaction temperature was changed from 60 to 80 °C, although the higher studied reaction temperature
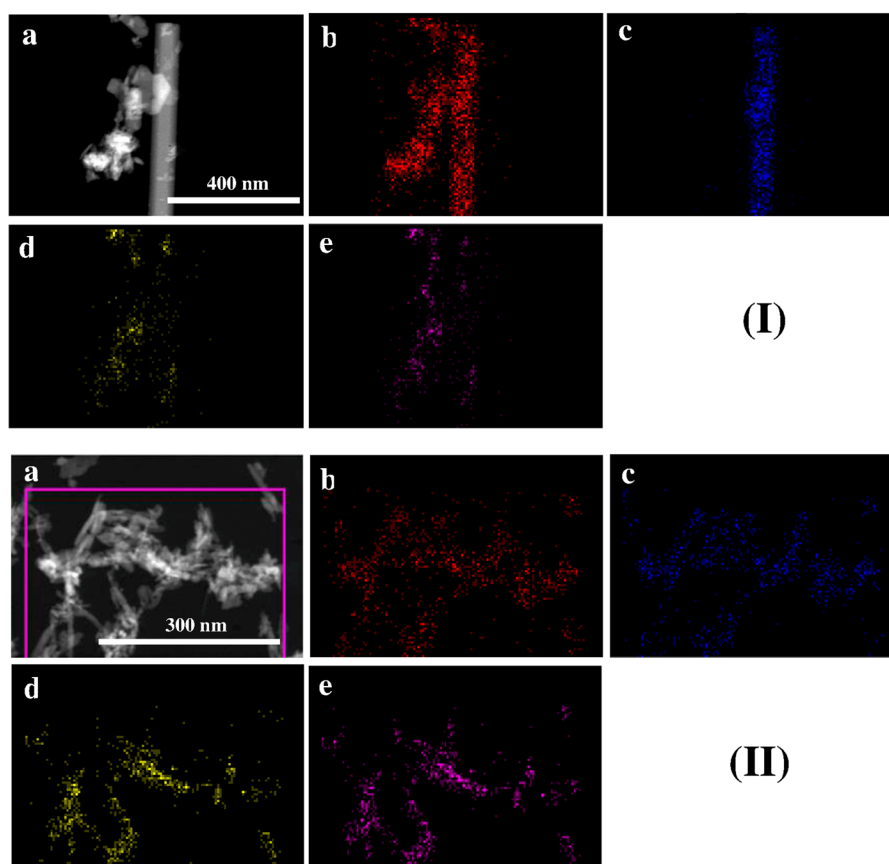
Figure 2. (I) EDS elemental mapping of HAp−TiO$_2$-2 nanocomposites: (a) selected area of the sample, (b) O mapping, (c) Ti mapping, (d) P mapping, and (e) Ca mapping. (II) EDS elemental mapping of HAp−TiO$_2$-h nanocomposites: (a) selected area of the sample, (b) O mapping, (c) Ti mapping, (d) P mapping, and (e) Ca mapping.

(80 °C) gave nanoplates with smaller dimensions and higher surface areas. SEM analysis of the composite samples revealed that the initial concentration of TIP plays an important role in determining the morphology of the resulting nanocomposites. For 80 °C and 6000 psi with initial concentration of 1.1 mol l^{-1} TIP (HAp−TiO$_2$-1), HAp nanoplates with 50−200 nm width and TiO$_2$ particles having a thick sheet-type structure with 200 nm width and 1−2 μm length were obtained (Figure 1d). At higher TIP concentration (1.5 mol/L), HAp nanoplates were formed on the surface of well-separated TiO$_2$ nanorods, which are 50−300 nm in diameter and 1−4 μm in length, as seen in the SEM and TEM images of HAp−TiO$_2$-2 in Figure 1e,g. The effect of the reaction pressure on the morphology of the nanocomposites was studied by changing the pressure from 6000 to 8000 psi, while remaining the temperature at 80 °C and the initial TIP concentration of 1.5 mol l^{-1}. SEM analysis of the HAp−TiO$_2$-3 (prepared at 8000 psi) shows that the reaction pressure did not have a strong influence on the morphology of the synthesized particulates (data not shown here). On the other hand, using the hydrothermal technique resulted in the formation of oblong-shaped particles, as shown in Figure 1f,h.

3.2. EDS Analysis of HAp and HAp−TiO$_2$ Nanocomposites. Energy-dispersive spectroscopy (EDS) was employed for mapping Ca, P, Ti, and O in the synthesized HAp−TiO$_2$ nanocomposites. Figure 2 clearly demonstrates the presence of O, Ti, P, and Ca in the nanocomposites. From the EDS elemental mapping of HAp−TiO$_2$-2 nanocomposites (Figure 2I), the rod-like morphology is clear, showing the presence of Ti,

the major elemental component of TiO$_2$, in the composites (Figure 2I, panel c). It can also be seen that Ca and P (Figure 2I, panels e and d, respectively), found exclusively in HAp, are homogeneously distributed on the TiO$_2$ surface. This helps to confirm that the nanoplates are HAp grown on the surface of TiO$_2$ rods.

EDX elemental mapping of HAp−TiO$_2$-h nanocomposites demonstrates a relatively homogeneous distribution of Ti, P, and Ca throughout the composite material (Figure 2II, panels c, d, and e, respectively). Thus, it can also be concluded that the oblong-shaped particles of TiO$_2$ and HAp are uniformly and homogeneously distributed within the synthesized nanocomposites.

The EDS spectra for HAp-2 and HAp−TiO$_2$-2 are shown in Figure 3. The investigation confirms the existence of Ca, P, O, and C elements for HAp-2 (Figure 3a) and Ca, P, O, Ti, and C elements in the synthesized HAp−TiO$_2$-2 nanocomposites (Figure 3b). The Ca/P atomic ratio for HAp-1 and HAp-2 powders (Table 2) indicates a predominately stoichiometric HAp crystal, as the measured ratio was close to 1.67. In addition, no noticeable difference was found for the Ca/P ratios of the HAp−TiO$_2$ nanocomposites synthesized at different conditions (reaction temperature, reaction pressure, and initial concentration of TIP) and HAp−TiO$_2$-h nanocomposites, exhibiting a lowered Ca/P atomic ratio, likely reflecting higher PO$_4$$^{3-}$ content.

3.3. XRD Analysis of HAp and HAp−TiO$_2$ Nanocomposites. Figure 4 shows the XRD patterns for the HAp-2 and HAp−TiO$_2$-2 and HAp−TiO$_2$-h nanocomposites in the 2θ
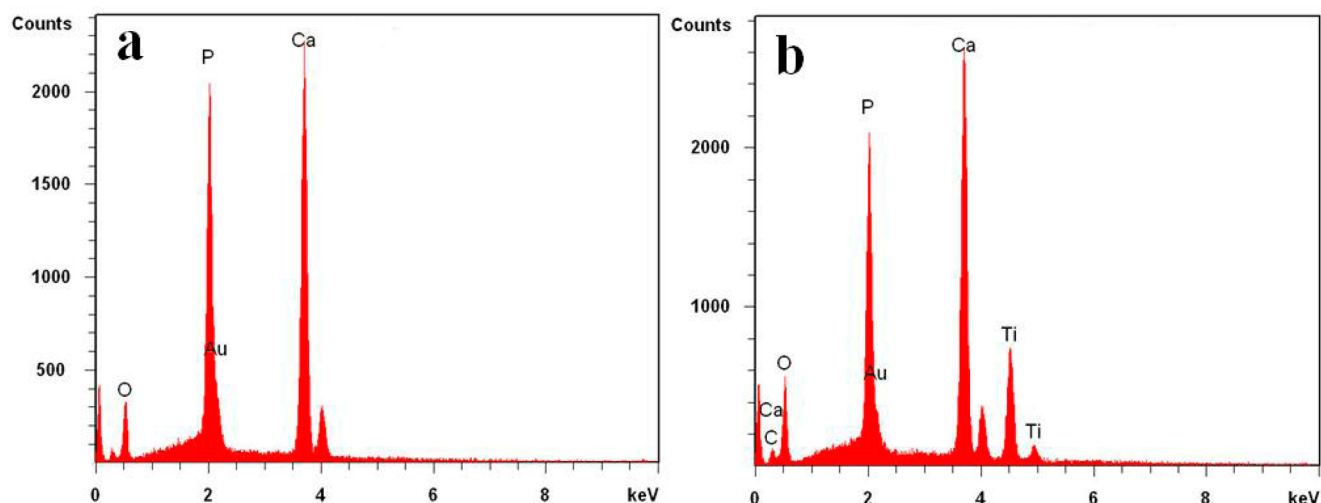
Figure 3. EDS spectra of the (a) HAp-2 and (b) HAp−TiO$_2$-2 nanocomposites.

Table 2. Ca/P Atomic Ratios for HAp and HAp−TiO$_2$ Nanocomposites

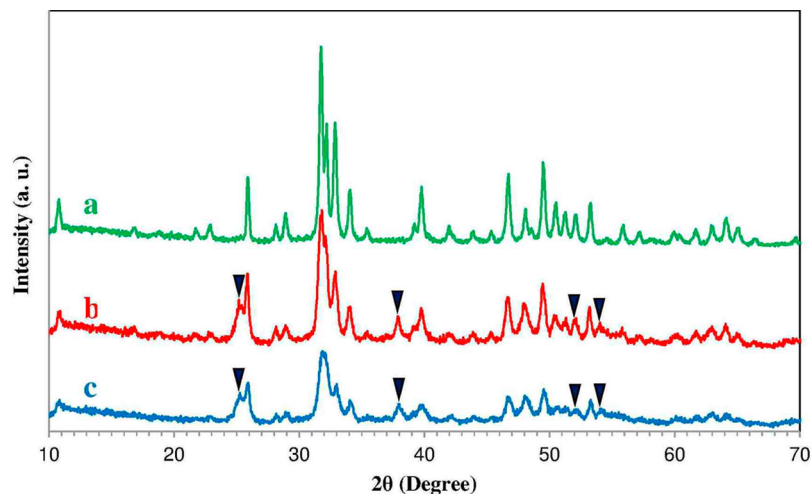|	atomic %			
	Ca	P	Ca/P	Ti
HAp-1	21.9 ± 1.2	13.5 ± 1.7	1.62 ± 0.22	
HAp-2	24.7 ± 2.3	15.0 ± 1.3	1.65 ± 0.21	
HAp−TiO$_2$-1	27.4 ± 1.8	17.2 ± 1.6	1.59 ± 0.18	5.8 ± 1.2
HAp−TiO$_2$-2	27.6 ± 1.9	17.8 ± 1.3	1.55 ± 0.16	7.8 ± 1.1
HAp−TiO$_2$-3	25.1 ± 2.2	16.5 ± 1.8	1.52 ± 0.21	5.9 ± 0.1
HAp−TiO$_2$-h	21.9 ± 1.4	14.6 ± 0.9	1.50 ± 0.13	4.9 ± 0.1

Figure 4. XRD patterns of the (a) HAp-2, (b) HAp−TiO$_2$-2, and (c) HAp−TiO$_2$-h nanocomposites. (b and c) Filled triangles (▼) represent the prominent characteristic peaks of anatase TiO$_2$.

range of 10−70°. In the XRD pattern of HAp-2 (Figure 4a), all the diffraction peaks correspond to hexagonal HAp according to JCPDS: 09−432.[5] No impurities are observed in the pattern, indicating pure HAp. In Figure 4b,c (for HAp−TiO$_2$ nanocomposites), the XRD patterns show all the diffraction peaks for HAp, along with new intensive peaks at $2\theta \approx 25.2°$, 37.7°, 53.8°, and 55° (shown by ▼) which are the prominent characteristic peaks of anatase TiO$_2$ assigned to the diffraction of (101), (004), (105), and (211) planes of TiO$_2$ anatase phase, respectively, confirming the incorporation of titania into the HAp matrix. This perfectly coincides with the anatase TiO$_2$

JCPDS card data (file no. 21-1272). Meanwhile, the peak at 47.9° is consistent with (213) Bragg reflection of HAp and (200) plane of TiO$_2$ anatase.[5,21,31] From the XRD patterns, it can be concluded that the unique HAp−TiO$_2$ nanocomposites maintain HAp crystal phase without phase transformation. Under the examined experimental conditions, the HAp precursor is stable, with TIP precursors grown to form anatase TiO$_2$ rod-like crystals. For the composite samples, the intensity of the TiO$_2$ peaks increases with the increase of the TiO$_2$ content, while the intensity of the HAp peaks decreases, as distinguishable in the XRD pattern of HAp−TiO$_2$-2 nanocomposites
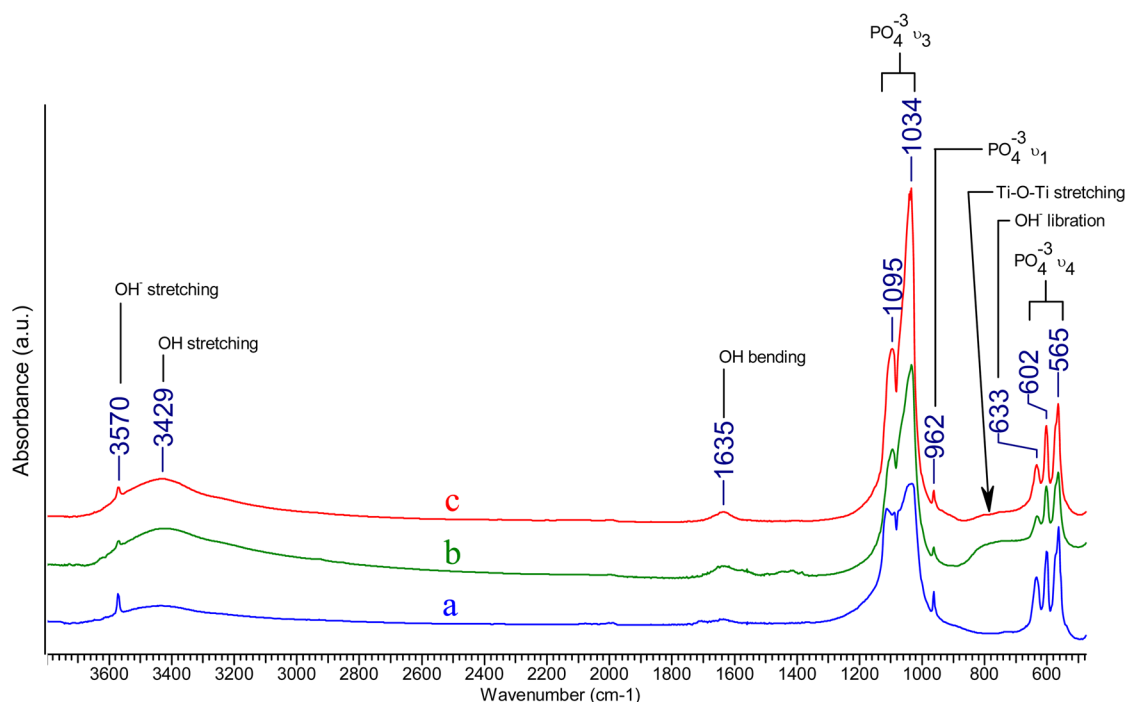
Figure 5. FTIR spectra of the (a) HAp-2, (b) HAp−TiO$_2$-2, and (c) HAp−TiO$_2$-h nanocomposites.

(Figure 4b) compared to the HAp−TiO$_2$-h nanocomposite (Figure 4c).

3.4. FTIR Spectroscopy of HAp and HAp−TiO$_2$ Nanocomposites.
The synthesized HAp and HAp−TiO$_2$ nanocomposites were also analyzed by FTIR. The FTIR spectra of HAp-2 nanoplates and HAp−TiO$_2$-2 and HAp−TiO$_2$-h nanocomposites are displayed in Figure 5. Several characteristic peaks of HAp are present in all the three spectra at 3570, 1095, 1034, 962, 633, 602, and 565 cm^{-1}. The peaks at 3570 and 633 cm^{-1} are attributed to the stretching and libration bands originating from the OH$^-$ ion, while the characteristic bands of PO$_4^{3-}$ ion appear at 1095 and 1034 (v_3), 962 (v_1), and 602 and 565 cm^{-1} (v_4).[32−34] The well-preserved characteristic peaks of HAp in the spectra of HAp−TiO$_2$ nanocomposites suggest no significant structural change or transformation of HAp throughout nanocomposite formation. This is challenging to obtain by using other synthesis methods, showing the utility of the examined approach. The broad peaks at 3429 and 1635 cm^{-1} in Figure 5a are attributable to the O−H stretching and bending modes of the surface-absorbed water, respectively. These peaks became more evident in the spectra of the synthesized HAp−TiO$_2$ nanocomposites (Figure 5b,c), also attributable to the structural hydroxyl group in the nano TiO$_2$.[35] In comparison to the spectrum of HAp (Figure 5a), there is an extra broad peak in the region of 600−800 cm^{-1} in the spectra of HAp−TiO$_2$ nanocomposites (Figure 5b,c), with the spectrum of HAp−TiO$_2$-2 (Figure 5b) being more evident. This broad peak may be due to the Ti−O−Ti band of TiO$_2$ as revealed by XRD.[36] Hence, the FTIR results confirm the presence of TiO$_2$ with intact HAp in the synthesized HAp−TiO$_2$ nanocomposites.

3.5. BET Analysis of HAp and HAp−TiO$_2$ Nanocomposites Synthesized in Supercritical CO$_2$.
The BET isotherms for pure HAp-2 and HAp−TiO$_2$-2 nanocomposites are plotted in Figure 6, curves a and b, respectively. Both isotherms correspond to type IV isotherms (IUPAC classification)
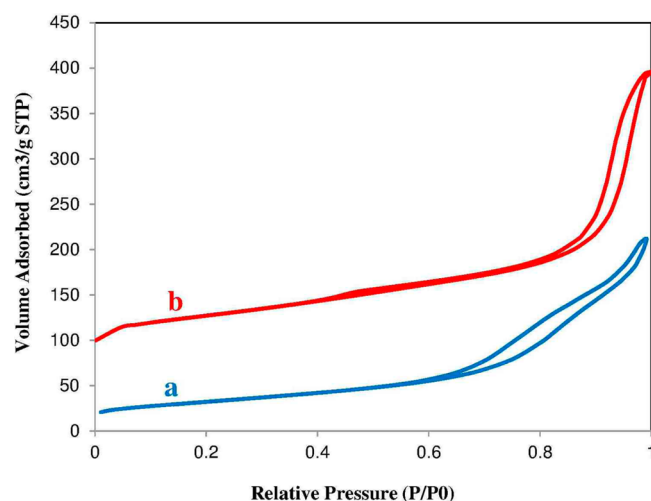

Figure 6. N$_2$ adsorption/desorption isotherms for (a) HAp-2 and (b) HAp−TiO$_2$-2 nanocomposites.

with a capillary condensation step above 0.4 P/P0, which is typical of mesoporous structures.[37,38] According to the IUPAC classification, the isotherms have a type H3 hysteresis loop with the continuous nitrogen uptake at very high relative pressure that is associated with aggregates of plate-like HAp particles giving rise to slit-shaped pores.[39] The HAp−TiO$_2$ nanocomposites show a significantly higher specific surface area, close to 170 m^2/g, with very homogeneous mesopores that are clearly distinguished from the macropores, as confirmed by its N$_2$ physisorption isotherm (Figure 6b). Adsorption in the low relative pressure region (0−0.4) is attributed to the micropores. The first hysteresis loop in the P/P0 range of 0.4−0.6 corresponds to the small size mesopores generated from the void space between the HAp crystallites.[39] Moreover, it exhibits another distinguished steep increase in the adsorption starting at P/P0 of 0.8. This nitrogen uptake at very
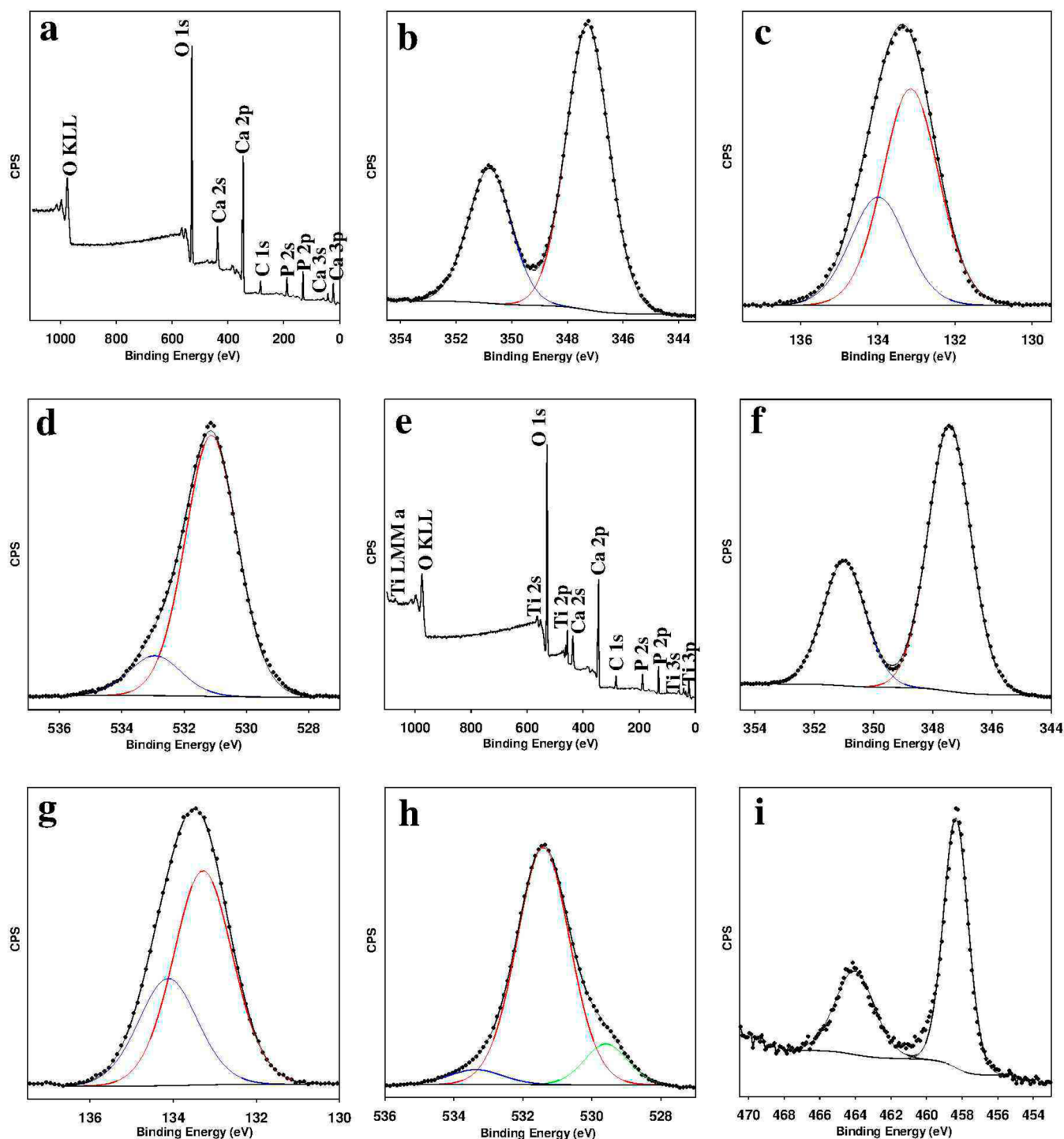
Figure 7. (a) XPS survey spectrum of the HAp-2 and high-resolution XPS scan of the (b) Ca 2p, (c) P 2p, and (d) O 1s regions for HAp-2. (e) XPS survey spectrum of the HAp−TiO$_2$-2 and high-resolution XPS scan of the (f) Ca 2p, (g) P 2p, (h) O 1s, and (i) Ti 2p regions for HAp−TiO$_2$-2.

high relative pressure corresponds to the formation of macropores that start filling only at high P/P0, close to 1.0. The observed macroporosity can be attributed to the voids between agglomerations of plate-like HAp primary particles, likely between the secondary particles.[40] Pure HAp-2 exhibits a surface area of about 72 m^2/g, which when compared with HAp−TiO$_2$ nanocomposites, showed a wide distribution of the pores and larger average pore diameter, as shown in Figure 6a. The capillary condensation step is much more pronounced and shifted to higher relative pressures, 0.6−0.8, for pure HAp with

respect to that of HAp−TiO$_2$ composite, which reveals the dominance of larger mesopores.[37] The SEM micrographs of pure HAp, Figure 1c, show aggregates of porous secondary particles. Compared with the HAp−TiO$_2$ composite, the aggregates are larger, 0.3−0.8 μm, indicating the presence of larger and less homogeneous macropores. Therefore, it is suggested that in the case of HAp−TiO$_2$ nanocomposite, the HAp agglomerates forming the slit-like pores tend to diminish in population and size. Also, the volume of the intercrystallite HAp space is reduced, so it could be concluded that the mesopore

size of HAp is altered upon formation of TiO_2. Farhangi and Charpentier synthesized TiO_2 nanowires on the graphene sheets in $scCO_2$, reporting similar results.[41]

3.6. XPS Analyses of HAp and HAp−TiO₂ Nanocomposites Synthesized in Supercritical CO₂. XPS analysis was performed on the HAp and HAp−TiO₂ samples, and the core level spectra (high-resolution XPS scan of the Ca 2p, P 2p, O 1s, and Ti 2p region) is depicted in Figure 7. As illustrated in the survey scans (Figure 7a,e), only Ca, P, O, and C for HAp-2 and Ca, P, O, Ti, and C for HAp−TiO₂-2 nanocomposites were identified. The respective atomic percentages for these elements are provided in Table 3. Carbon

Table 3. XPS Atomic Percentages for HAp-2 and HAp−TiO₂-2 Samples

	atomic %				
	Ca	P	O	C	Ti
HAp-2	19.3	11.9	57.5	11.3	
TiO₂−HAp-2	15.2	10.6	57.9	11.9	4.5
			TiO₂　HAp, OH		
			6.72　　51.18		

concentrations of 11.3 and 11.9% were observed in HAp-2 and HAp−TiO₂-2 composites, respectively, which is considered to be typical for organic contamination on clean surfaces.[18] This contamination may result from the chemisorption of CO_2 molecules from the atmosphere or from the reaction under $scCO_2$, unreacted acetic acid, and washing with $scCO_2$. In the recorded spectrum for HAp-2, the high-resolution XPS scan of the Ca 2p region (Figure 7b) represents two peaks for Ca 2p1/2 and Ca 2p3/2 at binding energies of 350.80 and 347.28 eV, respectively, which are assigned to hydroxyapatite. In the high-resolution P 2p XPS scan of HAp (Figure 7c), two peaks for P 2p1/2 and P 2p3/2 are observed at 134.99 and 133.15 eV, respectively, which are attributed to HAp. Figure 7d shows the high-resolution XPS scan of the O 1s region with peaks at binding energies of 532.93 and 531.12 eV that correspond to adsorbed water in the hydroxyapatite crystal and phosphate group, respectively.[11] The calculated Ca/O and Ca/P ratios for the HAp-2 are 0.34 and 1.62, respectively, which are very close to the theoretical values of 0.38 and 1.67 for HAp. The high-resolution XPS record of Ca 2p region of HAp−TiO₂ (Figure 7f) shows peaks for Ca 2p1/2 and Ca 2p3/2 at bonding energies of 350.99 and 347.44 eV, respectively, and that of P 2p represents two peaks for P 2p1/2 and P 2p3/2 at 134.12 and 133.28 eV, respectively (Figure 7g). These peak positions coincide well with the Ca and P in hydroxyapatite, as explained earlier, and only the negligible difference in binding energies of Ca 2p and P 2p core levels indicates the formation of HAp with similar stoichiometries in both HAp-2 and HAp−TiO₂-2 nanocomposite. The O 1s XPS spectrum (Figure 7h) can be deconvoluted into three distinct peaks, indicating the presence of various O states on the surface.[42] The subpeak at a binding energy of 529.59 eV is attributed to the lattice oxygen atoms TiO_2 (Ti−O bonds), while the subpeak at 533.36 eV corresponds to adsorbed water in the HAp crystal, and the other peak at 531.41 eV is due to the contribution of OH^- groups on the surface, phosphate group, or defective oxide sites. In Figure 7i, the core level spectrum of Ti 2p shows two peaks for Ti 2p3/2 and Ti 2p1/2 at binding energies of 458.35 and 464.02 eV, respectively. These are attributed to Ti in the 4+ state,[43]

indicating that the Ti detected in the TiO₂−HAp nanocomposites is only the oxide, TiO_2, obtained from the TIP hydrolyzed in the synthesis procedure. These XPS results help to confirm the formation of hydroxyapatite and titania in the HAp−TiO₂ nanocomposites. It can also be concluded that the HAp−TiO₂ nanocomposite is stable under the examined reaction conditions. The calculated Ca/O and Ca/P ratios for the HAp−TiO₂-2 composite are 0.3 and 1.43, respectively, which are very close to the theoretical values.[18]

Compared to the theoretical value for Ca/O ratio, 0.38, the calculated Ca/O ratio for the HAp−TiO₂-2 composite corresponds to the oxygen excess. This is attributed to the presence of OH groups on the surface, as Ti−OH remains in the sol−gel prepared materials promoting the osteointegration process.[18] Therefore, the XPS results suggest that the prepared HAp−TiO₂ composites may exhibit enhanced bioactive properties. Future investigation of the in vitro biocompatibility of the synthesized nanocomposites is planned as the next stage of this work.

3.7. XANES Spectroscopies of TiO₂, HAp, and HAp−TiO₂ Nanocomposites Synthesized in Supercritical CO₂. Figure 8 shows the Ti $L_{3,2}$-edge XANES of the HAp−TiO₂-2
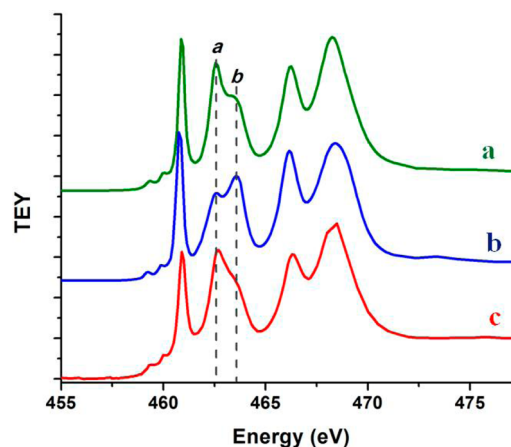

Figure 8. Ti $L_{3,2}$-edge XANES spectra of the (a) TiO_2 nanoparticles calcined at 450 °C, (b) TiO_2 nanoparticles calcined at 750 °C, and (c) HAp−TiO₂-2 nanocomposite.

nanocomposites in comparison with TiO_2 nanoparticles synthesized in supercritical CO_2 following the procedure presented in Salarian et al.[30] after calcination at 450 and 750 °C as standard samples. XRD studies of the TiO_2 nanoparticles showed that the as-prepared materials transferred from the amorphous to anatase phase during heat treatment at 450 °C, while after calcination at 750 °C, the transformation from anatase to rutile occurs (data not shown here). Characteristic features of TiO_2 that come from Ti 2p to 3d transitions are observed in the Ti $L_{3,2}$-edge XANES spectra. For TiO_2 standard samples, the peaks in the XANES spectra are due to the splitting pattern (t_{2g} and e_g) of the energy of the d orbitals under an octahedral crystal field followed by local distortion that leads to different local symmetries for anatase (D_{2d}) and rutile (D_{2h}). We can see that the most striking difference is the intensity ratio between feature a and b, that is, feature a is dominant in anatase (Figure 8a) while feature b in rutile (Figure 8b). The lowering of the O_h symmetry to D_{2d} and D_{2h} leads to the $2p \rightarrow e_g$ transition further splitting into peak a and b at the L_3-edge. The symmetry variations between anatase and rutile have an impact on the e_g

state; therefore, we can track anatase and rutile phases via the relative ratio between features *a* and *b* (Figure 8).[44,45] The spectrum of the HAp−TiO$_2$-2 nanocomposites (Figure 8c) illustrates well-resolved features of anatase TiO$_2$ that is confidently identified via the intensity ratio between *a* and *b*. It indicates that the TiO$_2$ in the nanocomposites is of anatase phase, which is consistent with the XRD results.

Figure 9 shows the Ca L$_{3,2}$-edge XANES spectra of the HAp−TiO$_2$-2 nanocomposites and HAp-2 powders. Sharp
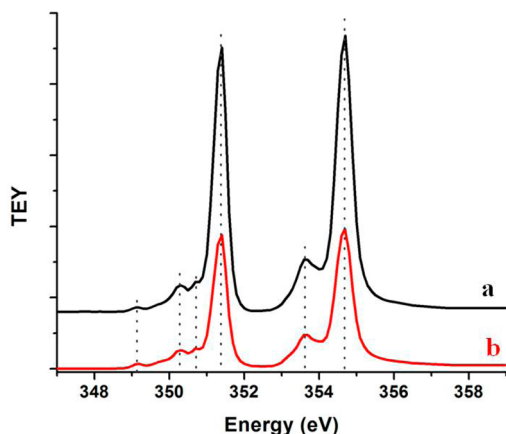

Figure 9. Ca L$_{3,2}$-edge XANES spectra of the (a) HAp and (b) HAp− TiO$_2$-2 nanocomposite powders.

peaks are observed at 351.4 and 354.7 eV, which come from the transitions of 2p$_{3/2}$ and 2p$_{1/2}$ electrons to the empty 3d state of Ca^{2+} ion that yields this spin−orbit doublet. The XANES spectrum of HAp−TiO$_2$-2 nanocomposites (Figure 9b) shows the same features to that of HAp-2 (Figure 9a), indicating that HAp was formed in the sample. Ca L$_{3,2}$-edge XANES results agree with the XRD results.

Figure 10I shows the O K-edge XANES spectra of the HAp−TiO$_2$-2 nanocomposites in comparison with those of HAp-2, anatase, and rutile TiO$_2$. The features originate from the transitions of O 1s to 2p (for TiO$_2$, O 2p states are hybridized with Ti 3d states). It can be seen that the spectrum of the HAp−TiO$_2$-2 nanocomposites (Figure 10I, spectrum b) shows the features of both anatase TiO$_2$ and HAp (e.g., peaks *a* and *c* are from anatase TiO$_2$, and peaks *b*, *d*, and *e* are from HAp). It agrees well with the Ti L$_{3,2}$-edge and Ca L$_{3,2}$-edge XANES results, confirming that the prepared sample contains both anatase TiO$_2$ and HAp. Because the edge jump of the XANES spectrum is proportional to the quantities of the sample, the compositional fractions of the HAp−TiO$_2$-2 nanocomposites can be obtained by fitting a linear combination of the spectra of their components to that of the composites. Figure 10II displays the linear fitting results of the HAp−TiO$_2$-2 nanocomposites. The fitting curve (red dash-dotted curve) is in good agreement with the experimental data (black solid curve), illustrating that the weight ratio between anatase TiO$_2$ and HAp is about 1:1.6. This also implies that the nanocomposite is uniform in the area being probed.

3.8. TGA of HAp and HAp−TiO$_2$ Nanocomposites. The thermal analysis of the HAp-2 powder and HAp−TiO$_2$-2 and HAp−TiO$_2$-h nanocomposites was performed under flowing air from room temperature to 1200 °C by TGA, as illustrated in Figure 11. The TGA curve of pure HAp is divided into four stages, as illustrated in Figure 11a. The first stage, from room
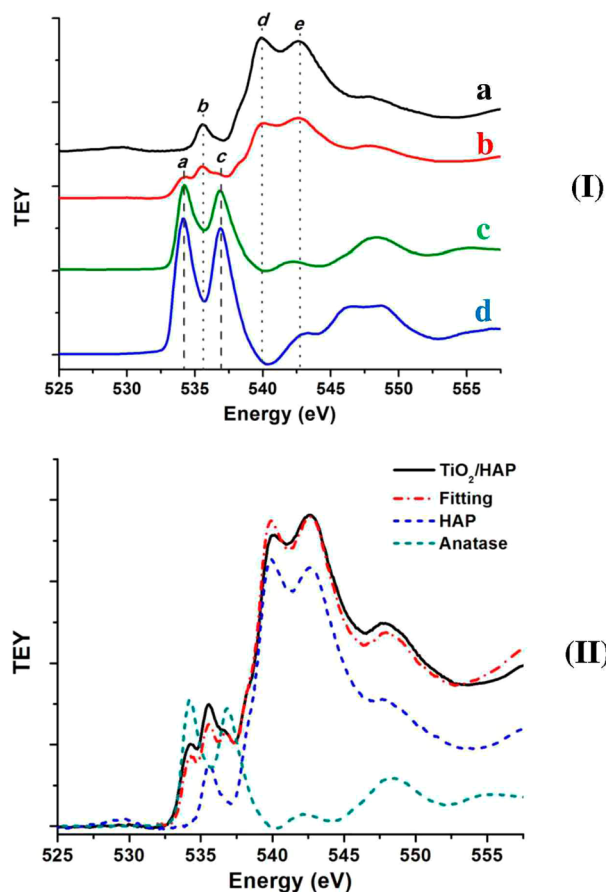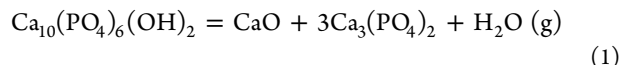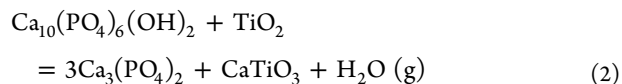

Figure 10. (I) O K-edge XANES spectra of the (b) HAp−TiO$_2$-2 nanocomposites in comparison with (a) HAp-2, (c) TiO2 nanoparticles calcined at 450 °C, and (d) TiO2 nanoparticles calcined at 750 °C. (II) O K-edge linear fitting of the HAp−TiO$_2$-2 nanocomposites.

temperature to 240 °C, corresponds to the evaporation of the physically absorbed water of the product. The second stage, from 240 to 440 °C, is attributed to the combustion and carbonization of organic substances such as CTAB and unreacted acetic acid. The third stage, from 440 to 550 °C, is caused by the decomposition of residual organic materials. Another endothermic transition takes place between 550 and 1100 °C, with a peak at 800 °C attributed to the partial decomposition of HAp to low-temperature phase of tricalcium phosphate (*β*-TCP). It has been reported that HAp is likely to decompose at 800−900 °C in air and 950 °C in vacuum,[46,47] and the following chemical reaction is proposed:

$$Ca_{10}(PO_4)_6(OH)_2 = CaO + 3Ca_3(PO_4)_2 + H_2O \text{ (g)}$$

(1)

For TiO$_2$−HAp nanocomposites, the increase in peak area of the peak at 800 °C as compared to pure HAp is due to both the partial dissociation of HAp to TCP and the conversion of anatase TiO$_2$ to the rutile phase of TiO$_2$ crystal, as the transformation from anatase to rutile occurs at temperatures between 400 and 1000 °C.[12] Moreover, it has been reported that the reaction between HAp and TiO$_2$ is feasible and expected to happen at the temperature above ~750 °C, and *β*-TCP and CaTiO$_3$ are formed.[47] The related chemical reaction is as follows:
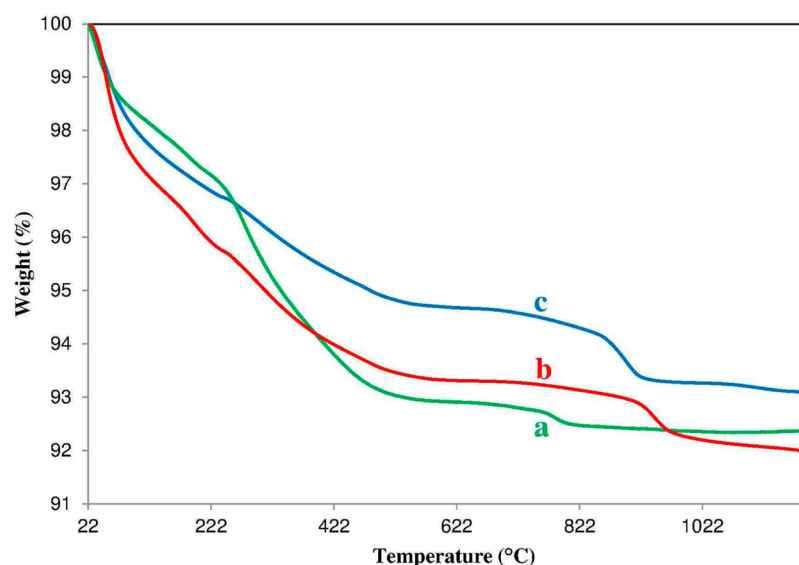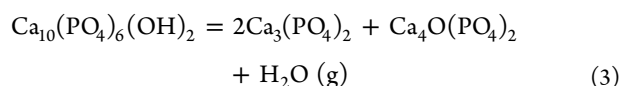
$$Ca_{10}(PO_4)_6(OH)_2 + TiO_2$$
$$= 3Ca_3(PO_4)_2 + CaTiO_3 + H_2O \text{ (g)}$$

(2)

16927

dx.doi.org/10.1021/am5044888 | *ACS Appl. Mater. Interfaces* 2014, 6, 16918−16931

Figure 11. TGA spectrum of (a) HAp-2, (b) HAp–TiO$_2$-2 nanocomposites, and (c) HAp–TiO$_2$-h nanocomposites.

Table 4. Mechanical Properties of PCL/HAp and PCL/HAp–TiO$_2$ Composites

PCL:HAp-2 (w/w)	PCL:HAp–TiO$_2$-2 (w/w)	PCL: HAp–TiO$_2$-h (w/w)	Young's modulus (MPa)	tensile strength (MPa)	offset yield 1% (MPa)	flexural modulus (MPa)	flexural strength (MPa)
100:0			155.2 ± 24.5	9.3 ± 2.9	5.0 ± 0.9	247.0 ± 28.5	13.2 ± 1.6
100:10			379.6 ± 16.2	10.9 ± 2.5	7.1 ± 0.3	551.0 ± 16.8	16.3 ± 0.3
100:20			352.8 ± 16.3	7.1 ± 0.9	5.3 ± 0.4	485.8 ± 23.6	16.6 ± 2.2
100:30			238.2 ± 11.5	6.5 ± 1.4	5.4 ± 1.6	425.0 ± 32.7	11.4 ± 0.6
	100:10		355.2 ± 13.2	12.0 ± 3.6	6.2 ± 0.9	744.6 ± 25.8	18.2 ± 2.6
	100:20		665.5 ± 24.6	15.8 ± 0.9	10.6 ± 0.9	716.3 ± 14.6	26.5 ± 0.7
	100:30		467.0 ± 62.0	11.5 ± 1.9	7.4 ± 0.7	512.0 ± 24.3	17.4 ± 0.9
		100:20	241.8 ± 25.6	6.2 ± 2.0	5.0 ± 2.7	423.6 ± 35.4	10.8 ± 1.7

There is another possibility of formation of TCP through the direct dissociation of HAp, as it can dissociate to Ca-orthophosphate and TCP by the following reaction:

$$Ca_{10}(PO_4)_6(OH)_2 = 2Ca_3(PO_4)_2 + Ca_4O(PO_4)_2$$
$$+ H_2O \text{ (g)} \qquad (3)$$

The Ca-orthophosphate formed as a result of reaction 3 subsequently reacts with TiO$_2$, leading to the formation of TCP and CaTiO$_3$.[47] The suggested reaction could be

$$Ca_4O(PO_4)_2 + TiO_2 = CaTiO_3 + Ca_3(PO_4)_2 \qquad (4)$$

From the above discussion, the weight changes in this region should therefore be correlated with TiO$_2$ phase transformation and TCP and CaTiO$_3$ formation (eqs 2−4). Because TCP formation is widely reported in all the HAp–TiO$_2$ compositions at or above 900 °C, it is highly likely that the weight loss must be due to TCP formation by reaction (eq 2), while CaTiO$_3$ formation does not produce a recordable weight change. In any case, the CaTiO$_3$ formation can be described by two possible reactions (eqs 2 and 4). So, it could be concluded that the presence of the titania modifies the thermal behavior with respect to the pure HAp.

3.9. Mechanical Properties of PCL/HAp and PCL/HAp–TiO$_2$ Composites. The mechanical properties (Young's modulus and ultimate tensile strength) of PCL/HAp and PCL/HAp–TiO$_2$ composites comprising 0−30% (w/w) HAp and HAp–TiO$_2$ synthesized by the combined coprecipitation and

sol−gel method and hydrothermal process were investigated. An exponential increase in the Young's modulus of PCL/HAp-2 and PCL/HAp–TiO$_2$-2 was observed with the increase in HAp-2 and HAp–TiO$_2$-2 concentrations, respectively. For example, the 20% (w/w) HAp–TiO$_2$-2 added composite possesses the highest Young's modulus of 665.5 MPa, which provides a 4-fold increase from pure PCL. Moreover, the ultimate tensile strength showed little variation between examined material groups, while a noticeable trend was observed with respect to loading concentration. It was shown that the tensile strength of PCL/HAp decreased from 9.3 for unfilled PCL to 6.5 MPa for PCL/HAp with increasing the amount of filler, HAp-2, to 30%. In other words, the greater HAp-2 content results in an increase in the brittle nature of the composites. On the contrary, a significant increase occurred in the tensile strength of the PCL/HAp–TiO$_2$ composites to 12.0 and 15.8 MPa for samples loaded with 10−20% (w/w) HAp–TiO$_2$. On the other hand, compared to PCL/HAp–TiO$_2$-h composite specimen containing 20% (w/w) HAp–TiO$_2$-h, PCL/HAp–TiO$_2$-2 composite clearly exhibits higher modulus and higher maximum tensile strength. The strengthening effects observed for PCL/HAp–TiO$_2$-2 composite over the PCL/HAp–TiO$_2$-h composite were concluded to be due to the morphology, size, and preferred orientation. The comparison of the mechanical properties of our resulting nanocomposites to the work of others is complicated by the different measurement techniques utilized; although, compared to that of cortical and cancellous bone, the tensile strength of our PCL/HAp–TiO$_2$-2 composites is
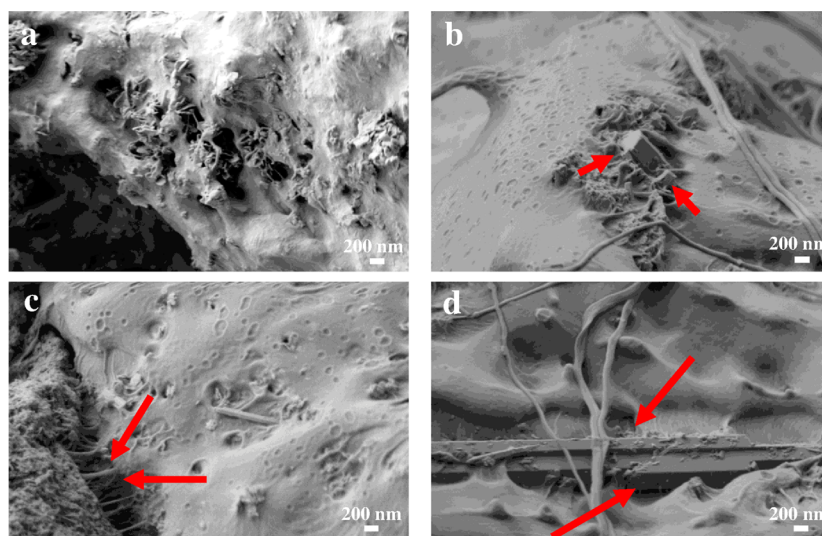
Figure 12. SEM images of the fracture surfaces of (a) PCL/HAp and (b−d) PCL/HAp−TiO$_2$ containing 20 wt % HAp−TiO$_2$. Short arrows indicate nanorods pullout, and long arrows indicate crack bridging by the TiO$_2$ nanorods.

considered to be sufficient enough to preserve their structure and mechanical integrity for predictable times, even under load-bearing conditions.

In addition, the flexural modulus and flexural strength values of composites reflect their resistance to flexural loading, which is a combination of tension and compression forces. Similarly, dramatic reinforcements in the flexural properties (FS and FM) were achieved for PCL/HAp−TiO$_2$-2 composites, as evident in Table 4. PCL/HAp−TiO$_2$-2 composite formulation containing 20 wt % HAp−TiO$_2$-2 exhibited a roughly 3-fold increase in flexural modulus and a 2-fold increase in flexural strength compared to those of blank PCL. This extraordinary mechanical reinforcement provided by PCL/HAp−TiO$_2$-2 composites exceeded the enhancements observed with PCL/HAp-2 composites, indicating the importance of mechanical coupling between the TiO$_2$ nanorods and the PCL matrix.

The SEM micrographs of the fracture surfaces of the PCL/HAp−TiO$_2$ nanocomposite loaded with 20 wt % HAp−TiO$_2$ are shown in Figure 12. It can be seen that the nanocomposite loaded with 20 wt % HAp−TiO$_2$ exhibited a rough surface with partially broken or pulled out TiO$_2$ rodlike structures on their surface, shown by the arrows in Figure 12b. This nanorod "pullout" effect would provide a strong interfacial shear strength between the TiO$_2$ nanorods and PCL matrix from the high surface area of the nanorods. Moreover, it is clear from Figure 12b,d that there is a strong adhesion between the HAp−TiO$_2$ and PCL matrix, as these partially pulled out TiO$_2$ nanorods take part in bridging the crack during propagation and bridge the cracks in the matrix, as shown in Figure 12c. Conversely, the unfilled PCL matrix displays a very smooth fracture plane with the cracks propagating without any hindrance (data not shown here).

4. CONCLUSION

A novel combined coprecipitation and sol−gel method in the green solvent supercritical carbon dioxide (scCO$_2$) was successfully applied to derive an innovative HAp-titania bioceramic with excellent chemical and structural uniformity. PCL/HAp−TiO$_2$ composites with significantly improved physical and mechanical properties suitable for tissue engineering were designed as described above. The results demonstrated that the morphology of the unique HAp−TiO$_2$ composites can be customized by adjusting the experimental conditions, particularly the initial concentration of TIP and the reaction temperature. The formed HAp−TiO$_2$ nanocomposites with a higher surface area and greater thermal stability compared to HAp nanoparticles are particularly attractive as reinforcing fillers for biodegradable synthetic polymers. With a loading of 20% (w/w) TiO$_2$−HAp, the obtained nanocomposites exhibited a tensile modulus of 665.5 MPa, which is more than a 4-fold increase compared to that of blank polymer. The presented work suggests that these unique PCL/HAp−TiO$_2$ nanocomposites with enhanced mechanical properties demonstrate the potential use of this synthetic approach for bone tissue engineering applications.

AUTHOR INFORMATION

Corresponding Author
*E-mail: pcharpentier@eng.uwo.ca.

Notes
The authors declare no competing financial interest.

REFERENCES

(1) Jevtic, M.; Mitric, M.; Skapin, S.; Jancar, B.; Ignjatovic, N.; Uskokovic, D. Crystal Structure of Hydroxyapatite Nanorods Synthesized by Sonochemical Homogeneous Precipitation. *Cryst. Growth Des.* **2008**, *8*, 2217−2222.

(2) Sun, Y.; Guo, G.; Tao, D.; Wang, Z. Reverse Microemulsion-Directed Synthesis of Hydroxyapatite Nanoparticles under Hydrothermal Conditions. *J. Phys. Chem. Solids* **2007**, *68*, 373−377.

(3) Wang, Y.; Zhang, S.; Wei, K.; Zhao, N.; Chen, J.; Wang, X. Hydrothermal Synthesis of Hydroxyapatite Nanopowders using Cationic Surfactant as a Template. *Mater. Lett.* **2006**, *60*, 1484−1487.

(4) Xiao, X.; Liu, R.; Zheng, Y. Characterization of Hydroxyapatite/ Titania Composite Coatings Codeposited by a Hydrothermal− Electrochemical Method on Titanium. *Surf. Coat. Technol.* **2006**, *200*, 4406−4413.

(5) Joseph Nathanael, A.; Mangalaraj, D.; Chen, P. C.; Ponpandian, N. Mechanical and Photocatalytic Properties of Hydroxyapatite/ Titania Nanocomposites Prepared by Combined High Gravity and Hydrothermal Process. *Compos. Sci. Technol.* **2010**, *70*, 419−426.

(6) Costa, D. O.; Dixon, S. J.; Rizkalla, A. S. One- and Three-Dimensional Growth of Hydroxyapatite Nanowires during Sol−Gel−Hydrothermal Synthesis. *ACS Appl. Mater. Interfaces* **2012**, *4*, 1490−1499.

(7) Lin, K.; Chang, J.; Cheng, R.; Ruan, M. Hydrothermal Microemulsion Synthesis of Stoichiometric Single Crystal Hydroxyapatite Nanorods with Mono-Dispersion and Narrow-Size Distribution. *Mater. Lett.* **2007**, *61*, 1683−1687.

(8) Liu, Y.; Hou, D.; Wang, G. A Simple Wet Chemical Synthesis and Characterization of Hydroxyapatite Nanorods. *Mater. Chem. Phys.* **2004**, *86*, 69−73.

(9) Salarian, M.; Solati-Hashjin, M.; Shafiei, S. S.; Goudarzi, A.; Salarian, R.; Nemati, A. Surfactant-Assisted Synthesis and Characterization of Hydroxyapatite Nanorods under Hydrothermal Conditions. *Mater. Sci.−Pol.* **2009**, *27*, 961−971.

(10) Salarian, M.; Solati-Hashjin, M.; Shafiei, S. S.; Salarian, R.; Nemati, Z. A. Template-Directed Hydrothermal Synthesis of Dandelion-like Hydroxyapatite in the Presence of Cetyltrimethylammonium Bromide and Polyethylene Glycol. *Ceram. Int.* **2009**, *35*, 2563−2569.

(11) Pushpakanth, S.; Srinivasan, B.; Sreedhar, B.; Sastry, T. An In Situ Approach to Prepare Nanorods of Titania−Hydroxyapatite (TiO₂−HAp) Nanocomposite by Microwave Hydrothermal Technique. *Mater. Chem. Phys.* **2008**, *107*, 492−498.

(12) Fidancevska, E.; Ruseska, G.; Bossert, J.; Lin, Y.-M.; Boccaccini, A. R. Fabrication and Characterization of Porous Bioceramic Composites Based on Hydroxyapatite and Titania. *Mater. Chem. Phys.* **2007**, *103*, 95−100.

(13) Sato, M.; Aslani, A.; Sambito, M. A.; Kalkhoran, N. M.; Slamovich, E. B.; Webster, T. J. Nanocrystalline Hydroxyapatite/ Titania Coatings on Titanium Improves Osteoblast Adhesion. *J. Biomed. Mater. Res., Part A* **2008**, *84*, 265−272.

(14) Kim, H. W.; Kim, H. E.; Salih, V.; Knowles, J. C. Hydroxyapatite and Titania Sol−Gel Composite Coatings on Titanium for Hard Tissue Implants; Mechanical and in Vitro Biological Performance. *J. Biomed. Mater. Res., Part B* **2005**, *72*, 1−8.

(15) Oktar, F. Hydroxyapatite−TiO₂ Composites. *Mater. Lett.* **2006**, *60*, 2207−2210.

(16) Kim, H. M.; Chae, W. P.; Chang, K. W.; Chun, S.; Kim, S.; Jeong, Y.; Kang, I. K. Composite Nanofiber Mats Consisting of Hydroxyapatite and Titania for Biomedical Applications. *J. Biomed. Mater. Res., Part B* **2010**, *94*, 380−387.

(17) Wakamura, M. Photocatalysis by Calcium Hydroxyapatite Modified with Ti(IV). *Fujitsu Sci. Tech. J.* **2005**, *41*, 181−190.

(18) Milella, E.; Cosentino, F.; Licciulli, A.; Massaro, C. Preparation and Characterisation of Titania/Hydroxyapatite Composite Coatings Obtained by Sol−Gel Process. *Biomaterials* **2001**, *22*, 1425−1431.

(19) Im, K. H.; Lee, S. B.; Kim, K.-M.; Lee, Y.-K. Improvement of Bonding Strength to Titanium Surface by Sol−Gel Derived Hybrid Coating of Hydroxyapatite and Titania by Sol−Gel Process. *Surf. Coat. Technol.* **2007**, *202*, 1135−1138.

(20) Anmin, H.; Tong, L.; Ming, L.; Chengkang, C.; Huiqin, L.; Dali, M. Preparation of Nanocrystals Hydroxyapatite/TiO₂ Compound by Hydrothermal Treatment. *Appl. Catal., B* **2006**, *63*, 41−44.

(21) Siddharthan, A.; Kumar, T.; Seshadri, S. In Situ Composite Coating of Titania−Hydroxyapatite on Commercially Pure Titanium by Microwave Processing. *Surf. Coat. Technol.* **2010**, *204*, 1755−1763.

(22) Pai, R. A.; Humayun, R.; Schulberg, M. T.; Sengupta, A.; Sun, J. N.; Watkins, J. J. Mesoporous Silicates Prepared using Preorganized Templates in Supercritical Fluids. *Science* **2004**, *303*, 507−510.

(23) Sui, R.; Rizkalla, A. S.; Charpentier, P. A. Formation of Titania Nanofibers: A Direct Sol−Gel Route in Supercritical CO₂. *Langmuir* **2005**, *21*, 6150−6153.

(24) Lucky, R. A.; Charpentier, P. A. A One-Step Approach to the Synthesis of ZrO₂-Modified TiO₂ Nanotubes in Supercritical Carbon Dioxide. *Adv. Biomater.* **2008**, *20*, 1755−1759.

(25) Lucky, R.; Charpentier, P. A Thermal Study on the Structural Changes of Bimetallic ZrO₂-Modified TiO₂ Nanotubes Synthesized using Supercritical CO₂. *Nanotechnology* **2009**, *20*, 195601.

(26) Lucky, R. A.; Charpentier, P. A. N-Doped ZrO₂/TiO₂ Bimetallic Materials Synthesized in Supercritical CO₂: Morphology and Photocatalytic Activity. *Appl. Catal., B* **2010**, *96*, 516−523.

(27) Allo, B. A.; Rizkalla, A. S.; Mequanint, K. Hydroxyapatite Formation on Sol−Gel Derived Poly (ε-caprolactone)/Bioactive Glass Hybrid Biomaterials. *ACS Appl. Mater. Interfaces* **2012**, *4*, 3148−3156.

(28) Allo, B. A.; Rizkalla, A. S.; Mequanint, K. Synthesis and Electrospinning of ε-polycaprolactone-Bioactive Glass Hybrid Biomaterials via a Sol−Gel Process. *Langmuir* **2010**, *26*, 18340−18348.

(29) Allo, B. A.; Lin, S.; Mequanint, K.; Rizkalla, A. S. Role of Bioactive 3D Hybrid Fibrous Scaffolds on Mechanical Behavior and Spatiotemporal Osteoblast Gene Expression. *ACS Appl. Mater. Interfaces* **2013**, *5*, 7574−7583.

(30) Salarian, M.; Xu, W. Z.; Biesinger, M. C.; Charpentier, P. A. Synthesis and Characterization of Novel TiO2-Poly(propylene fumarate) Nanocomposites for Bone Cementation. *J. Mater. Chem. B* **2014**, *2* (32), 5145−5146.

(31) Kuroda, K.; Shidu, H.; Ichino, R.; Okido, M. Formation of Titania/Hydroxyapatite Composite Films by Pulse Electrolysis. *Mater. Trans.* **2007**, *48*, 322−327.

(32) Fowler, B. Infrared Studies of Apatites. I. Vibrational Assignments for Calcium, Strontium, and Barium Hydroxyapatites Utilizing Isotopic Substitution. *Inorg. Chem.* **1974**, *13*, 194−207.

(33) Park, E.; Condrate, R. A., Sr.; Lee, D. Infrared Spectral Investigation of Plasma Spray Coated Hydroxyapatite. *Mater. Lett.* **1998**, *36*, 38−43.

(34) Rapacz-Kmita, A.; Ślósarczyk, A.; Paszkiewicz, Z.; Paluszkiewicz, C. Phase Stability of Hydroxyapatite−Zirconia (HAp−ZrO₂) Composites for Bone Replacement. *J. Mol. Struct.* **2004**, *704*, 333−340.

(35) Soler-Illia, G. d. A.; Louis, A.; Sanchez, C. Synthesis and Characterization of Mesostructured Titania-based Materials Through Evaporation-Induced Self-Assembly. *Chem. Mater.* **2002**, *14*, 750−759.

(36) Mohan, L.; D, D.; Geetha, M.; Sankara Narayanan, T. S. N.; Asokamani, R. Electrophoretic Deposition of Nanocomposite (HAp + TiO₂) on Titanium Alloy for Biomedical Applications. *Ceram. Int.* **2012**, *38*, 3435−3443.

(37) Tsoncheva, T.; Ivanova, L.; Paneva, D.; Mitov, I.; Minchev, C.; Fröba, M. Cobalt and Iron Oxide Modified Mesoporous Zirconia: Preparation, Characterization, and Catalytic Behaviour in Methanol Conversion. *Microporous Mesoporous Mater.* **2009**, *120*, 389−396.

(38) Sing, K. S. Reporting Physisorption Data for Gas/Solid Systems with Special Reference to the Determination of Surface Area and Porosity (Recommendations 1984). *Pure Appl. Chem.* **1985**, *57*, 603−619.

(39) Giannakopoulou, T.; Todorova, N.; Romanos, G.; Vaimakis, T.; Dillert, R.; Bahnemann, D.; Trapalis, C. Composite Hydroxyapatite/ TiO₂ Materials for Photocatalytic Oxidation of NOₓ. *Mater. Sci. Eng., B* **2012**, *177*, 1046−1052.

(40) Khaleel, A.; Al-Mansouri, S. Meso-Macroporous γ-Alumina by Template-free Sol−Gel Synthesis: The Effect of the Solvent and Acid Catalyst on the Microstructure and Textural Properties. *Colloids Surf., A* **2010**, *369*, 272−280.

(41) Farhangi, N.; Chowdhury, R. R.; Medina-Gonzalez, Y.; Ray, M. B.; Charpentier, P. A. Visible Light Active Fe Doped TiO₂ Nanowires Grown on Graphene using Supercritical CO₂. *Appl. Catal., B* **2011**, *110*, 25−32.

(42) Abbasi, S.; Bayati, M.; Golestani-Fard, F.; Rezaei, H.; Zargar, H.; Samanipour, F.; Shoaei-Rad, V. Micro Arc Oxidized HAp—TiO_2 Nanostructured Hybrid Layers—Part I: Effect of Voltage and Growth Time. *Appl. Surf. Sci.* **2011**, *257*, 5944−5949.

(43) Golestani-Fard, F.; Bayati, M.; Zargar, H.; Abbasi, S.; Rezaei, H. MAO-Preparation of Nanocrystalline Hydroxyapatite—Titania Composite Films: Formation Stages and Effect of the Growth Time. *Mater. Res. Bull.* **2011**, *46*, 2422−2426.

(44) de Groot, F. M. F.; Figueiredo, M. O.; Basto, M. J.; Abbate, M.; Petersen, H.; Fuggle, J. C. 2p X-ray Absorption of Titanium in Minerals. *Phys. Chem. Miner.* **1992**, *19*, 140−147.

(45) Liu, L.; Chan, J.; Sham, T.-K. Calcination-Induced Phase Transformation and Accompanying Optical Luminescence of TiO_2 Nanotubes: An X-ray Absorption Near-edge Structures and X-Ray Excited Optical Luminescence Study. *J. Phys. Chem. C* **2010**, *114*, 21353−21359.

(46) Cannillo, V.; Lusvarghi, L.; Sola, A. Production and Characterization of Plasma-Sprayed TiO_2—Hydroxyapatite Functionally Graded Coatings. *J. Eur. Ceram. Soc.* **2008**, *28*, 2161−2169.

(47) Nath, S.; Tripathi, R.; Basu, B. Understanding Phase Stability, Microstructure Development and Biocompatibility in Calcium Phosphate—Titania Composites, Synthesized from Hydroxyapatite and Titanium Powder Mix. *Mater. Sci. Eng., C* **2009**, *29*, 97−107.